

MeltpoolINR: Predicting temperature field, melt pool geometry, and their rate of change in laser powder bed fusion

Manav Manav^{1*†}, Nathanaël Perraudin^{2†}, Yunong Lin^{3†},
Mohamadreza Afrasiabi³, Fernando Perez-Cruz²,
Markus Bambach^{3*}, Laura De Lorenzis^{1*}

¹Computational Mechanics Group, ETH Zürich, Zürich, Switzerland.

²Swiss Data Science Center, ETH Zürich, Zürich, Switzerland.

³Advanced Manufacturing Lab, ETH Zürich, Zürich, Switzerland.

*Corresponding author(s). E-mail(s): mmanav@ethz.ch;
mbambach@ethz.ch; ldelorenzis@ethz.ch;

†These authors contributed equally to this work.

Abstract

We present a data-driven, differentiable neural network model designed to learn the temperature field, its gradient, and the cooling rate, while implicitly representing the melt pool boundary as a level set in laser powder bed fusion. The physics-guided model combines fully connected feed-forward neural networks with Fourier feature encoding of the spatial coordinates and laser position. Notably, our differentiable model allows for the computation of temperature derivatives with respect to position, time, and process parameters using autodifferentiation. Moreover, the implicit neural representation of the melt pool boundary as a level set enables the inference of the solidification rate and the rate of change in melt pool geometry relative to process parameters. The model is trained to learn the top view of the temperature field and its spatiotemporal derivatives during a single-track laser powder bed fusion process, as a function of three process parameters, using data from high-fidelity thermo-fluid simulations. The model accuracy is evaluated and compared to a state-of-the-art convolutional neural network model, demonstrating strong generalization ability and close agreement with high-fidelity data.

Keywords: Laser powder bed fusion, Melt pool, Deep learning, Implicit neural representation

1 Introduction

Laser powder bed fusion (LPBF) is a prominent metal additive manufacturing process for metal parts with complex geometries. It offers remarkable flexibility in fabricating customized parts with significantly reduced lead times compared to conventional manufacturing processes. For these reasons, it finds increasing application in biomedical, aerospace, automotive, and other high-tech industries [1–3]. In LPBF, part fabrication progresses through the sequential spreading of powder layers and their selective melting via a laser, leading to the formation of a melt pool, and subsequent solidification. Thus, the printing process involves complex multiscale and multiphysics phenomena, including laser beam-powder interaction and melt pool formation, melt pool dynamics, and fast cooling and solidification cycles [4].

The process is controlled by adjusting a number of parameters, including laser power, scanning speed, and preheating temperature, as well as the scanning strategy [5]. However, the inherent complexity of the involved physical mechanisms obscures the direct correlation between the process parameters and the quality of a fabricated part; thus, ensuring precise control over part quality remains challenging, rendering the printed parts susceptible to defects such as keyhole porosity, lack of fusion, and surface defects [6, 7].

This has motivated researchers to deepen their understanding of the underlying physics of the printing process [4, 8] and to develop reliable models and numerical methods to simulate, optimize, and control LPBF with computational tools [9–12]. In this direction, the first analytical model of the temperature field due to a moving point source, akin to the LPBF fabrication process, was developed by Rosenthal [13]. Semi-analytical models of temperature field due to a moving heat source by incorporating idealized boundary effects have also been developed [14]. These models are computationally efficient, but their accuracy is limited by strong simplifying assumptions such as neglecting the temperature dependence of material properties, the latent heat of fusion and the heat loss due to radiation and convection, and other simplifications regarding boundary conditions. Significant progress has also been made in detailed simulation of the LPBF process [8, 15, 16] using complex mathematical models discretized with numerical methods such as finite elements (FE) [17, 18], finite volumes [19, 20], smoothed particle hydrodynamics (SPH) [21–23], Lattice Boltzmann [24], and others. These approaches have simulated specific parts of the printing process and provided crucial insights into the physics of the process and explanations for the experimental observations. However, high-fidelity simulations are computationally very expensive, prohibiting their wider application in process optimization and control.

In recent years, machine learning models have seen tremendous growth in various scientific applications. They have been employed in learning from data as well as in the direct numerical solution of partial differential equations [25]. These models can be used for quick inference, enabling the possibility of optimization and control. This has led to a surge in research focused on employing machine learning for LPBF process modeling [26, 27]. In recognition of the importance of the temperature field during the printing process on the part quality, considerable effort has been directed toward machine learning models that can predict the temperature field in

and around the melt pool. The models presented in these works fall into two main categories: physics-informed and data-driven. A physics-informed approach that models heat transfer and melt pool fluid dynamics is presented in [28]. This model is not parametric, i.e. it solves the governing equations only for a prescribed set of process parameters like in a direct numerical simulation. A nonparametric PINNs approach solving only the heat conduction equation for the LPBF process is proposed in [29]. The authors also solve an inverse problem using PINNs to identify material properties from the partially observed temperature data. A parametric solution of the heat conduction equation for the LPBF process is obtained using PINNs in [30]. The proposed PINNs approaches have either modeled the physics adequately or obtained a parametric solution to only the heat conduction equation, but not both. Among the data-driven approaches, [31] proposes a method to learn the temperature field around the melt pool by learning a parametrization of isotherms and reconstruction of the temperature field through interpolation using data from thermal-fluid flow simulations. In [32], the temperature field obtained from the FE solution of only the heat transfer equation for a variety of scanning paths is learned using a combination of a recurrent neural network and a fully connected feed-forward network. Similarly obtained temperature field data for multilayer printing are learned using a fully connected feed-forward network in [33]. To accurately learn the temperature field in the melt pool from the high-fidelity data obtained from a computational fluid dynamics simulation, a model based on a convolutional neural network (CNN) is employed in [34]. In [35], an uncertainty-aware temperature model is proposed by combining physics-informed and parametric regressors utilizing heat transfer equation and experimental data.

In the LPBF process, the solidification of the melt pool typically entails high cooling rates and large thermal gradients which depend on the process parameters [36]. Notably, the cooling rates and thermal gradients near the melt pool boundary define the solidification rate and have significant influence on the microstructure [37–39] and on residual stresses [40–42], and consequently on the mechanical properties and geometric accuracy of the fabricated part [43]. The construction of a solidification map [44, 45] also relies on the knowledge of solidification rate and thermal gradient near the melt pool boundary. Furthermore, for a gradient-based optimization of the process parameters, the temperature field should be represented as a sufficiently smooth function of the spatiotemporal coordinates and of the process parameters, such that its derivatives can be computed accurately. Hence, a model that accurately predicts the temperature field, melt pool boundary, thermal gradient and cooling rate at the melt pool boundary, and their change due to a change in the process parameters is desired. However, none of the works in the literature has focused on the development of such a model. Notably, (semi)-analytical models yield such relations [13, 14], however, their accuracy is limited. As mentioned earlier, direct numerical solutions are not parametric and can provide accurate fields for only a prescribed set of process parameters, besides being computationally expensive. Parametric PINNs-based surrogate models [29, 30] can predict temperature field, thermal gradient, and cooling rate accurately and fast; however, they have not been employed for the prediction of melt pool evolution and its dependence on the process parameters. Furthermore, the

reported approaches model physics only partially i.e. they solve only the thermal conduction equation. Among the data-driven machine learning approaches [31–35], focus has been on learning the temperature field and not the thermal gradient and cooling rate. Also, they have not been applied to predict the melt pool evolution and its dependence on the process parameters.

In this paper, we propose an efficient data-driven approach by developing a differentiable model based on fully connected feed-forward neural networks, commonly known as multilayer perceptrons (MLPs), for learning the temperature field, thermal gradient, and cooling rate, inspired by the implicit neural representation of 3D objects [46]. We call our model MeltpoolINR which stands for “melt pool implicit neural representation”. Unlike CNNs, MeltpoolINR learns a resolution-independent continuous representation of the temperature field with advantages in the computation of the derivatives of the field and of the melt pool boundary. The inputs to the model are spatial coordinates, laser position, and the process parameters. We also employ Fourier feature encoding of coordinates and laser position which are well known to enable MLPs to learn sharp features in the data [47] such as in the temperature field and its derivatives near the melt pool boundary. Furthermore, to accurately capture the extremely sharp temperature variation at the front of the melt pool boundary, we include an exponential term in the expression for the temperature inspired by Rosenthal’s solution for a moving heat source [13]. Additionally, we employ the level-set method to represent the melt pool boundary implicitly and to model its evolution. We perform Sobolev training [48] of our model to learn the temperature field and its derivatives accurately using the high-fidelity physics-based data generated from SPH process simulations. In this work, we demonstrate the effectiveness of our approach in learning a 2D cross-section (top view) of the temperature field and its derivatives in single-track printing. The novel contributions of this work are threefold: (a) development of a differentiable neural network capable of learning the temperature field, thermal gradient and cooling rate, and providing the derivative of the temperature with respect to the process parameters using auto-differentiation, (b) implicit neural representation of the melt pool boundary as a level set to learn its evolution and infer solidification rate, and (c) inference of the rate of change of melt pool features with respect to the process parameters.

The remainder of this paper is organized as follows. The data generation method is briefly outlined in Section 2. The machine learning model and the level-set method are described in Section 3. The results are presented and discussed in Section 4. The paper ends with conclusions in Section 6.

2 Data generation

The dataset for training and validating the machine learning model is obtained by SPH numerical simulations. SPH, introduced in [49] and [50], is a particle-based numerical method widely used to solve differential equations describing large deformations, fluid flow, and phase transformations. In SPH, the continuum body is discretized into finite particles, whereby each particle interacts with its neighbors according to the governing

physical equations. Here, we use a thermo-fluid SPH approach, combined with a ray-tracing laser model introduced in [51], to simulate the single-track laser scanning process. As follows, we summarize the mathematical model and SPH discretization. For full details see [23, 51].

We simulate a laser scanning process over a single track, i.e. the elementary process into which an entire LPBF process can be decomposed. In total 210 simulations are performed for different values of the process parameters, i.e. laser power (P), laser scanning speed (v), and initial substrate temperature (T_{pre}), using all combinations of the values in Table 1. Here, the laser power and the laser scanning speed can be set in the LPBF machine for the scanning of individual tracks, whereas the initial substrate temperature represents the substrate heat accumulation by previous scanning. In the present study, we do not account for the randomly distributed particle geometry in the powder bed, in order to limit the computational cost. After the simulation, a post-processing step extracts the desired fields at the top surface from the SPH numerical results. The data for each case have the same dimension of [100, 128, 64] wherein 100 is the number of time steps and [128, 64] are the numbers of grid points in x and y directions (Figure 1), respectively.

Table 1 Values of the process parameters in the dataset.

Laser power (P) [W]	80, 120, 160, 200, 240, 280
Laser scanning speed (v) [m/s]	0.75, 1, 1.25, 1.5, 1.75, 2.25, 2.5
Initial substrate temperature (T_{pre}) [K]	300, 340, 380, 420, 460

In every simulated single-track process, a Gaussian laser beam with spot diameter $80 \mu\text{m}$ pointing vertically downwards scans the top surface of a Ti6Al4V substrate. The laser power and scanning speed do not change during each process. The substrate is simplified as a cuboid of dimensions $800 \times 400 \times 400 \mu\text{m}$, as shown in Figure 1a. The laser axis moves along the midline of the top surface of the substrate in the y direction, as depicted in Figure 1b. The scanning path is $600 \mu\text{m}$ long and its starting point is positioned with an offset of $100 \mu\text{m}$ to the left edge of the top surface. At the beginning of the process, the substrate has a uniform initial temperature. The material properties of the Ti6Al4V alloy for the simulations are listed in Table 2. The thermal conductivity and isobaric specific heat capacity are temperature-dependent and estimated using their values in the solid and liquid phases.

We solve the equations of incompressible fluid flow and heat transfer in the Lagrangian form:

$$\begin{cases} \frac{d\rho}{dt} = -\rho \nabla \cdot \mathbf{u} \\ \rho \frac{d\mathbf{u}}{dt} = -\nabla p + \mu \nabla^2 \mathbf{u} + \rho \mathbf{g} + \mathbf{b}^s + \mathbf{b}^w + \mathbf{b}^r \\ \rho c_p \frac{dT}{dt} = \nabla \cdot (k \nabla T) + \mathbf{T} : \nabla \mathbf{u} + q^{rc} + q^l + (q^b) \end{cases} \quad (1)$$

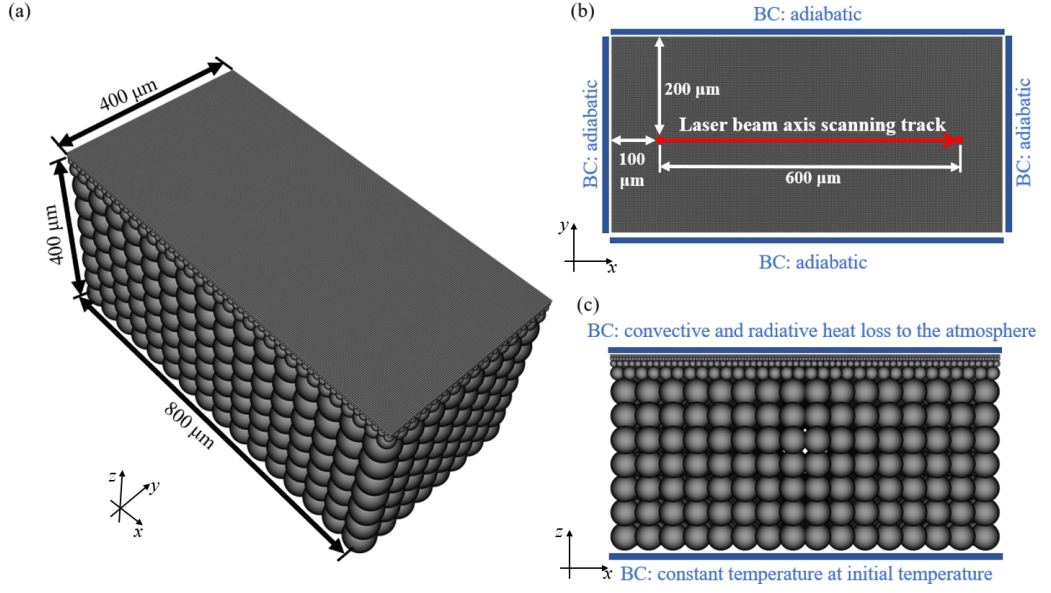


Fig. 1 SPH simulation setup: (a) geometry of the substrate; (b) boundary conditions on the lateral faces and laser beam axis scanning track; (c) boundary conditions on the top and bottom faces.

Table 2 Material properties of Ti6Al4V alloy and atmospheric conditions of the simulated process [51, 52].

Property / Atmospheric condition	Symbol	Value	Unit
Reference density	ρ_0	4420	kgm^{-3}
Solid thermal conductivity constant	k_S	33.4	$\text{Wm}^{-1}\text{K}^{-1}$
Liquid thermal conductivity constant	k_L	19	$\text{Wm}^{-1}\text{K}^{-1}$
Solid isobaric specific heat capacity constant	c_{pS}	830	$\text{Jkg}^{-1}\text{K}^{-1}$
Liquid isobaric specific heat capacity constant	c_{pL}	546	$\text{Jkg}^{-1}\text{K}^{-1}$
Dynamic viscosity	μ	0.005	$\text{kgm}^{-1}\text{s}^{-1}$
Surface tension	σ_T	1.493	Nm^{-1}
Surface tension gradient coefficient	σ'_T	1.9×10^{-4}	$\text{Nm}^{-1}\text{K}^{-1}$
Solidus temperature	T_S	1878	K
Liquidus temperature	T_L	1933	K
Reference temperature of evaporation	T_v	3133	K
Specific enthalpy of melting	H_m	2.9×10^5	Jkg^{-1}
Specific enthalpy of evaporation	H_v	9.83×10^6	Jkg^{-1}
Atmospheric pressure	P_{atm}	10^5	Pa
Atmospheric temperature	T_{atm}	300	K
Convective heat transfer coefficient	h_c	19	$\text{Wm}^{-2}\text{K}^{-1}$
Emissivity	ϵ	0.23	—
Molar mass	M_m	0.048	kgmol^{-1}

Here ρ denotes the density, t the time, \mathbf{u} the velocity, p the pressure, μ the dynamic viscosity, and \mathbf{g} the gravity acceleration. \mathbf{b}^s , \mathbf{b}^w and \mathbf{b}^r are the body forces induced respectively by surface tension, wetting effect, and recoil pressure of evaporation. c_p is the isobaric specific heat capacity, k the thermal conductivity, T the temperature,

and \mathbf{T} the shear stress tensor. q^{rc} is the heat loss induced by evaporation, q^l the laser heat input which is computed by a ray-tracing laser heat source model, and q^b is the heat loss induced by boundary conditions which is only applied to the surface.

As depicted in Figure 1b and Figure 1c, the four vertical faces of the substrate are subjected to adiabatic boundary conditions, hence $q^b = 0$. The top face experiences convective and radiative heat loss to the environment, with the atmospheric conditions in Table 2, hence

$$q^b = -\frac{h_c(T - T_{atm}) + \epsilon\sigma(T^4 - T_{atm}^4)}{\Delta x} \quad (2)$$

where h_c is the convective heat loss coefficient, T_{atm} the atmospheric temperature, ϵ the emissivity, σ the Stefan–Boltzmann constant, and Δx the minimum discretization spacing. The bottom face maintains a constant initial temperature. In the simulation, this boundary condition is achieved by adding two layers of ghost SPH particles below the substrate. During the time integration, the temperature of the ghost SPH particles remains the initial substrate temperature. The ghost particles thus conduct heat from interior SPH particles.

To reduce the computational cost, we deploy an adaptive spatial resolution scheme in SPH which refines and coarsens the particle cloud at selected time integration steps. The minimum discretization spacing of SPH is $6.3 \mu\text{m}$, and the time integration step is 6.3 ns .

The post-processing of the numerical solution follows three steps. First, from the SPH simulations, the fields at the 100 uniformly spaced time frames covering the whole process are saved to generate the 2D field data. Secondly, as Figure 2a depicts, the top surface particles for ray-tracing, which are determined by the method in [51], are filtered out and projected vertically onto a horizontal plane. A uniform 128×64 grid along the x and y directions is created on the horizontal plane. Thirdly, the 2D data consisting of the field variables on the grid points are computed by a 2D SPH interpolation with a renormalization denominator from the surface particles as follows:

$$f(\mathbf{x}_0)_{data} = \frac{\sum_j f(\mathbf{x}_j)_{SPH} W[|\mathbf{x}_0)_{data} - \mathbf{x}_j)_{SPH}|, h)] (V_j)_{SPH}}{\sum_j W[|\mathbf{x}_0)_{data} - \mathbf{x}_j)_{SPH}|, h)] (V_j)_{SPH}} \quad (3)$$

Here, $f(\mathbf{x}_0)_{data}$ is the value of a field variable at position $(\mathbf{x}_0)_{data}$, j denotes a particle in the neighborhood of $(\mathbf{x}_0)_{data}$ with position $(\mathbf{x}_j)_{SPH}$, and $W[\cdot, \cdot]$ is the kernel function, a weighting function whose value depends on $|\mathbf{x}_0)_{data} - \mathbf{x}_j)_{SPH}|$ and on the smoothing length h . The neighboring particles of $(\mathbf{x}_0)_{data}$ are the particles in the support domain of the kernel function $W(|\mathbf{x}_0)_{data} - \mathbf{x}|, h)$. $(V_j)_{SPH}$ is the volume of particle j . Here, we use as kernel function the 2D Wendland quintic function presented in [53] with a smoothing length of $4.725 \mu\text{m}$. Figure 2b schematically shows the relationship between top surface SPH particles and grid point at $(\mathbf{x}_0)_{data}$ in the SPH interpolation. Finally, at each time frame, field variables including the temperature T_{data} , the temperature gradient in x -direction $(\partial_x T)_{data}$, the temperature gradient in y direction $(\partial_y T)_{data}$, and the temporal temperature gradient $(\partial_t T)_{data}$ at the 2D uniform grid are generated (Figure 2c).

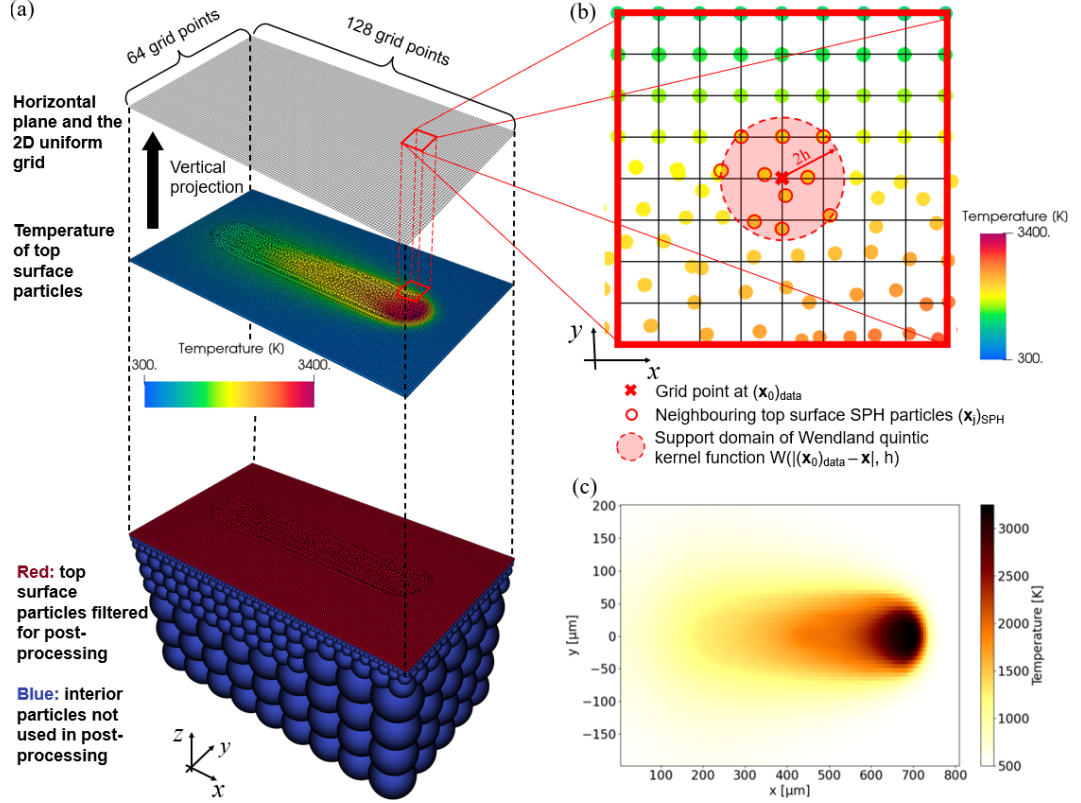


Fig. 2 Generation of temperature data for the dataset from SPH particles at one time frame; (a) vertical projection of filtered top surface particles to a uniform grid on a 2D plane; (b) computation of temperature at a grid point $(\mathbf{x}_0)_{data}$ by SPH interpolation; (c) post-processed temperature field data of dimension $[128, 64]$ at one time frame.

3 Methodology

In this section, we describe first our machine learning approach, and then the level set method, useful for the implicit representation of the melt pool.

3.1 Machine learning approach

We learn the top view of the temperature field, its gradient, and its time derivative in a single-track LPBF using a physics-guided Fourier feature network [46, 47, 54] based on MLPs, which we denote as MeltpoolINR (Implicit Neural Representation of the melt pool) (Figure 3). The architecture consists of four MLPs each employing the hyperbolic tangent (\tanh) activation function:

1. Spatial MLP: The inputs to this MLP are the transformed spatial coordinates of points in the printing domain and the laser position, x_l . First, the x -coordinate of points is transformed to the coordinate attached to the laser moving in the x -direction by setting $\xi = x - x_l$. Then Fourier feature mapping is applied to ξ , y ,

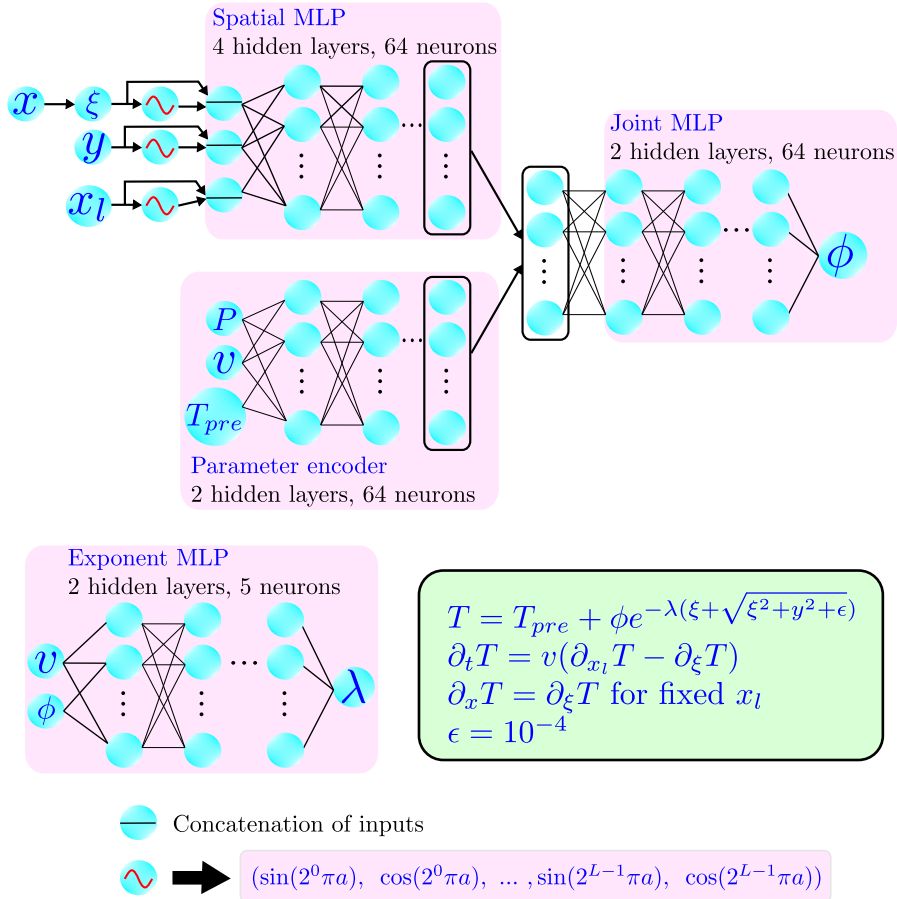


Fig. 3 The architecture of MelpoolINR with the Fourier feature mapping of the spatial coordinates and laser position.

and x_l and the input to the network is constructed by appending values of ξ , y , and x_l to their corresponding Fourier feature maps. The network consists of 4 hidden layers with 64 neurons in each layer.

2. Parameter encoder: This network takes the process parameters as input and encodes them in a latent space. It consists of 2 hidden layers with 64 neurons in each layer.
3. Joint MLP: The outputs of the Spatial MLP and the Parameter encoder are concatenated and supplied as input to this network. This network also consists of 2 hidden layers with 64 neurons in each layer.
4. Exponent MLP: Rosenthal's solution for a moving heat source [13] involves an exponential term in which the exponent includes laser velocity and thermal diffusivity. Here, we learn the exponent using a small MLP which consists of 2 hidden layers with 5 neurons in each layer.

The temperature field and its derivatives vary sharply near the melt pool boundary which is challenging for an MLP to learn. To overcome this, we augment the NN architecture with two features: (a) Fourier feature mapping, and (b) the inclusion of an exponential term in the output based on Rosenthal’s solution for a moving heat source [13]. Fourier feature mapping enables MLPs to learn high-frequency features and is extensively employed in computer vision for this purpose [46, 47, 54]. Furthermore, the sharply changing temperature field and its derivatives at the front of the melt pool still pose a challenge. To mitigate this, we include an exponential term in the expression for the temperature (see Figure 3) and learn the exponent from the data using an MLP. Note that the small parameter ϵ in the expression for the temperature smoothens the corner point, which would otherwise appear at $\xi = y = 0$. Furthermore, to enforce the physical constraint that the time derivative should be equal to the negative of the x-component of the temperature gradient times the scanning speed in the steady state (see A), we learn the temperature field in the coordinate system attached to the laser by setting $\xi = x - x_l$. The separation of MLPs for the dense spatial coordinates and the sparse parameter set is inspired from [54] and allowed us to learn using a smaller network.

We perform Sobolev training [48] of the network using the following loss function:

$$\mathcal{L} = \|T_\theta - T_{data}\| + w_x \|\partial_x T_\theta - (\partial_x T)_{data}\| + w_y \|\partial_y T_\theta - (\partial_y T)_{data}\| + w_t \|\partial_t T_\theta - (\partial_t T)_{data}\|, \quad (4)$$

where T_θ is the learned temperature, and $\partial_x T_\theta$, $\partial_y T_\theta$, and $\partial_t T_\theta$ are its derivatives with respect to x , y , and t , respectively, whereas T_{data} , $(\partial_x T)_{data}$, $(\partial_y T)_{data}$, $(\partial_t T)_{data}$ are provided in the dataset. For the loss weights, we set $w_x = w_y = w_t = 0$ for the first 50 epochs of training to focus on learning only the temperature field. After that, we change them to $w_x = 5$, $w_y = 1$ and $w_t = 5$.

To assess the accuracy of MeltpoolINR, we also train a CNN-based model. In the CNN, the temperature and its x , y , and t derivatives are the four independent network outputs, while the loss function remains the same as in (4). By treating the temperature and its derivatives as independent outputs, we allow the CNN to potentially overfit the data. The CNN, resembling the network in [55], comprises an MLP with 2 hidden layers and 1024 neurons followed by 5 sets of layers, each consisting of upsampling, convolution, and activation layers. We utilize Leaky ReLU as the activation function. See B for the details of the architecture. The CNN outputs a 4-channel field of 128×64 pixels, the four channels being the temperature and its x , y , and t derivatives. For this network, we set $w_x = w_y = w_t = 0.1$ in the loss function in (4).

In training, we employ the ADAM optimizer with a learning rate of 5×10^{-4} . We use MSE loss, as expressed below:

$$\|u\| = \frac{1}{n_{P3} n_{P2} n_{P1} n_t n_y n_x} \sum_{n=0}^{n_{P3}} \sum_{m=1}^{n_{P2}} \sum_{l=1}^{n_{P1}} \sum_{k=1}^{n_t} \sum_{j=1}^{n_y} \sum_{i=1}^{n_x} u(x^i, y^j, x_l^k, P_1^l, P_2^m, P_3^n)^2, \quad (5)$$

where n_x , n_y , n_t , n_{P_1} , n_{P_2} , and n_{P_3} are the numbers of grid points in the x , y , x_l , P_1 , P_2 , and P_3 directions, respectively. Also, for the CNN, x_l is replaced with t above. We randomly separate the data into training and testing cases, and use 90% of the data for training and the remaining 10% for testing.

3.2 Level set method

We aim to learn the geometry of the melt pool, its evolution over time, and its dependence on the process parameters. To accomplish this, we utilize an implicit representation of the melt pool boundary, expressed as the zero level-set of a level-set function $\phi(x, y, t, \mathbf{P})$, where x , y and t are the spatial and temporal coordinates, and \mathbf{P} denotes the vector of the process parameters. The evolution of ϕ is governed by the following equation [56]:

$$\frac{\partial \phi}{\partial t} + F|\nabla \phi| = 0, \quad (6)$$

where $F = F(x, y, t, \mathbf{P})$ is the speed function governing the evolution of the level set, ∇ denotes the spatial gradient, and $|\cdot|$ is the Euclidean norm. When ϕ is known and $|\nabla \phi| \neq 0$, (6) can be used to compute the speed function through:

$$F = -\frac{1}{|\nabla \phi|} \frac{\partial \phi}{\partial t}. \quad (7)$$

Since the isotherms at the solidus (T_S) and liquidus (T_L) temperatures define the melt pool boundary and the location of initiation of the solidification process, respectively, we define the level-set function using the temperature field as follows:

$$\phi = \frac{T}{T_0} - 1, \quad (8)$$

where one can set $T_0 = T_S$ to track the melt pool and $T_0 = T_L$ to track the initiation of the solidification process. The speed function F in the part of the isotherm at T_L , where the melt is solidifying, equals the solidification rate. For simplicity, we set $T_0 = (T_S + T_L)/2$ in this work.

The printing process can be optimized by controlling the melt pool geometry. The gradient-based optimization of the process parameters then requires the computation of the rate of change of the melt pool geometry and of its relevant features (i.e. width, length, aspect ratio) at a given time with respect to the process parameters. This computation is also facilitated by the level-set approach described by the following equation:

$$\frac{\partial \phi}{\partial P_i} + F_i^P |\nabla \phi| = 0, \quad (9)$$

where P_i is the i_{th} process parameter and $F_i^P \Delta P_i$ is the change in the melt pool boundary at the given time if one chooses $P_i + \Delta P_i$ as the process parameter instead of P_i (where ΔP_i is small). Consequently, the rate of change of the length (l), width (w), and aspect ratio ($AR = w/l$) of the melt pool with a change in the process parameter

P_i can be estimated via:

$$\frac{\partial l}{\partial P_i} = F_i^P(x_{\max}, y, t, \mathbf{P}) + F_i^P(x_{\min}, y, t, \mathbf{P}), \quad (10)$$

$$\frac{\partial w}{\partial P_i} = F_i^P(x, y_{\max}, t, \mathbf{P}) + F_i^P(x, y_{\min}, t, \mathbf{P}), \quad (11)$$

$$\frac{\partial (AR)}{\partial P_i} = \frac{1}{l} \left[\frac{\partial w}{\partial P_i} - AR \frac{\partial l}{\partial P_i} \right], \quad (12)$$

where we are assuming that the printing direction is parallel to the x axis (Figure 1), x_{\max} and x_{\min} are the x -coordinates of the extremes of the melt pool in the x direction, and y_{\max} and y_{\min} are the y -coordinates of the extremes of the melt pool in the y direction.

4 Results

This section presents the assessment of our proposed model and demonstrates the inference of the change in the melt pool geometry with the process parameters.

4.1 Assessment of the model

We evaluate the goodness of fit for field quantities using the coefficient of determination (R^2) values. To assess the accuracy of the prediction of the melt pool geometry, we utilize the Chamfer distance metric – see C.

Figure 4 shows the evaluation metrics computed on the test data set. Both models learn the temperature field accurately, but MeltpoolINR performs better than CNN in learning the temperature gradient and cooling rate, even though the CNN learns the temperature field and its spatial and temporal gradients as independent fields. Additionally, the gradients at the melt pool boundary are assessed. Here too, the performance of MeltpoolINR is better than the CNN. Furthermore, a comparison of the Chamfer distances for the two models shows that MeltpoolINR outperforms CNN. Even though the R^2 values for the temperature field predicted by MeltpoolINR and the CNN are comparable, the CNN performs comparatively poorly in learning the melt pool geometry.

Next, we investigate the spatial distribution of errors within the domain. Figure 5 compares the network outputs for a test case with the ground truth obtained from the SPH simulation. The error, defined as the difference between the network output and the ground truth, is also shown. We observe that while MeltpoolINR learns the melt pool boundary correctly, the CNN exhibits a pronounced step-like error profile. The fields obtained from the CNN have a comparatively higher error, as expected based on the goodness of fit shown in Figure 4. Furthermore, the errors are localized. As expected, the parts of the domain with steeper slopes of the temperature field are challenging to learn and errors are localized in those regions.

To investigate the error variation with the choice of the process parameters, we focus our attention on MeltpoolINR. Figure 6 shows the root mean squared error (RMSE) in the temperature field, and in its spatial and temporal gradients (see D

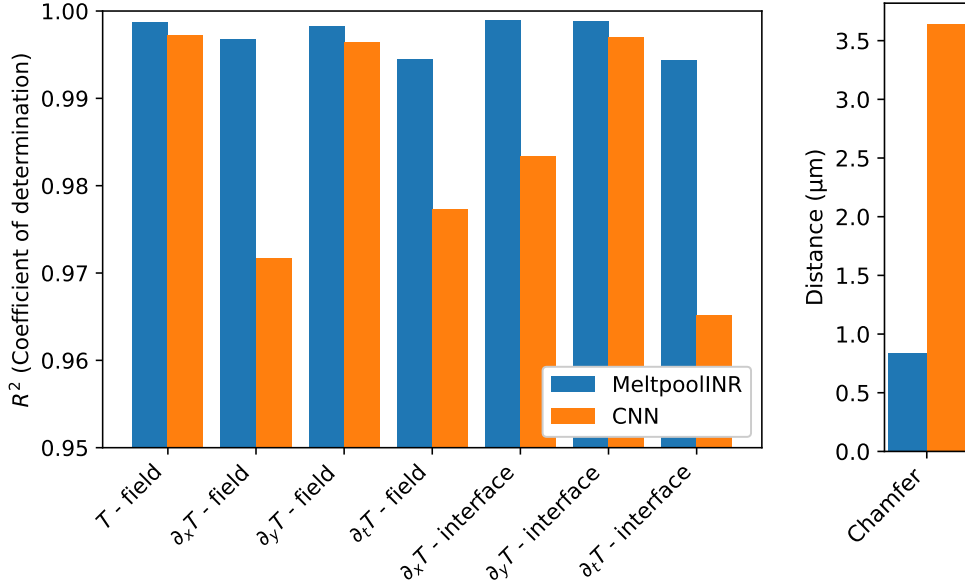


Fig. 4 Goodness of fit of the temperature field and its derivatives for the entire domain and at the melt pool boundary i.e. interface (left); Chamfer distance between the melt pool boundary in the data and the prediction (right).

for the errors for the complete set of process parameters). We observe that the errors in the test cases (shown by filled circles) are similar in magnitude to those of the surrounding training cases. This is an indicator of the generalizability of our model. The error increases for scenarios characterized by high power and low speed. This can be attributed to a qualitative change in the temperature profile indicated by the change in the melt pool shape. In contrast to other cases, the melt pool at high power and low speed is narrower at the front and wider at the back (see Figure E6).

We also assess the model performance in learning the melt pool boundary, as well as the temperature gradient and the cooling rate at the boundary, as shown in Figure 7. A comparison of the scale of the error bars between Figure 6 and Figure 7 reveals that the temperature gradient and the cooling rate at the boundaries are learned with significantly better accuracy. This observation is consistent with the spatial distribution of errors shown in Figure 5, which reveals that the errors are localized inside the melt pool for MeltpoolINR. Moreover, these errors do not exhibit a strong dependence on the laser power and scanning speed, unlike in Figure 6. However, the variation of the errors in the melt pool geometry with laser power and speed exhibits a similar pattern as observed in Figure 6.

4.2 Inference of the melt pool features

In this section, we demonstrate the capability of the model to predict the change in the melt pool geometry by predicting the solidification rate and the change in the melt pool length and aspect ratio when the process parameters are changed. First,

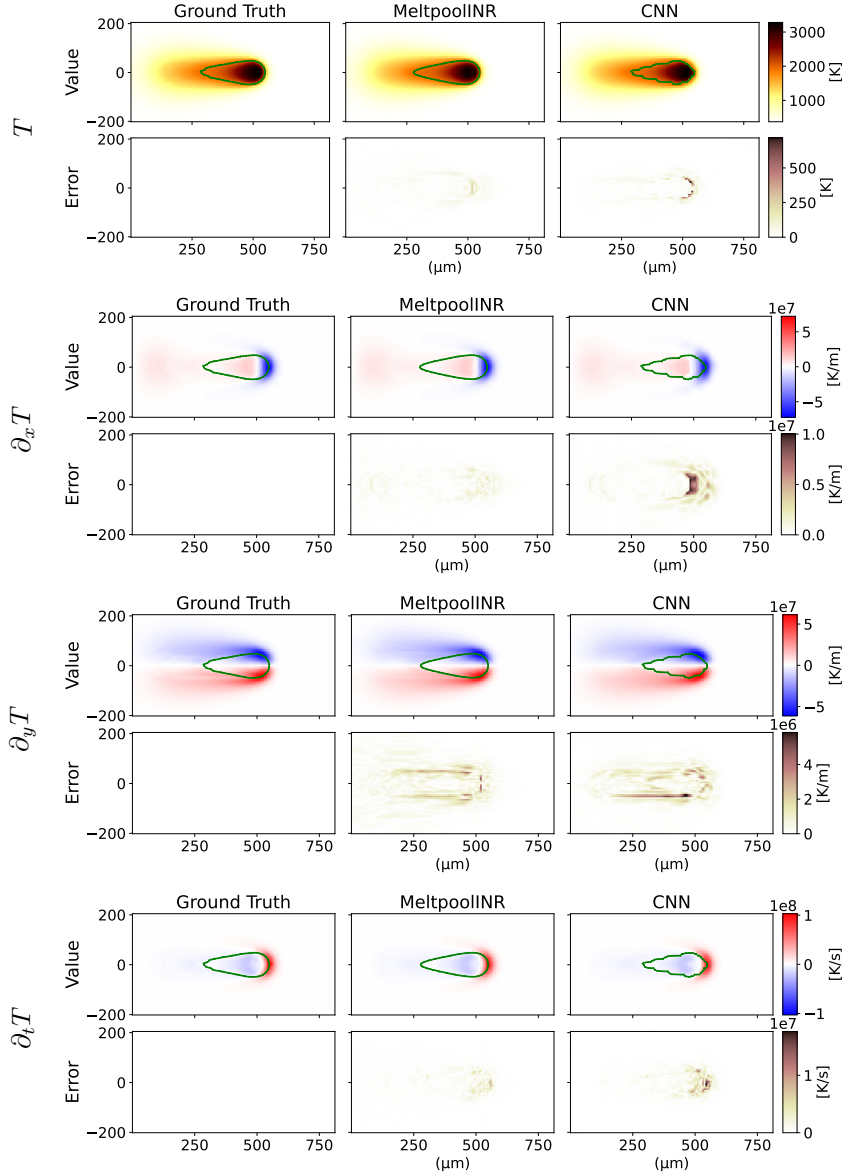


Fig. 5 Temperature field and its derivatives at time $202\mu\text{s}$ for a substrate preheating temperature of 380 K, laser power 160 W, and scanning speed 1.25 m/s. The difference between the ground truth and the outputs of the networks is also shown as an error.

we compute the speed function (F) at the melt pool boundary using (7), as shown in Figure 8. The melt pool boundary is parameterized by angle θ , as shown in the inset in Figure 8, to show the variation of F . F obtained from the simulation data and MeltpoolINR are in close agreement. Note that the noise in the simulation data arises due to the interpolation from the grid data required to determine the melt

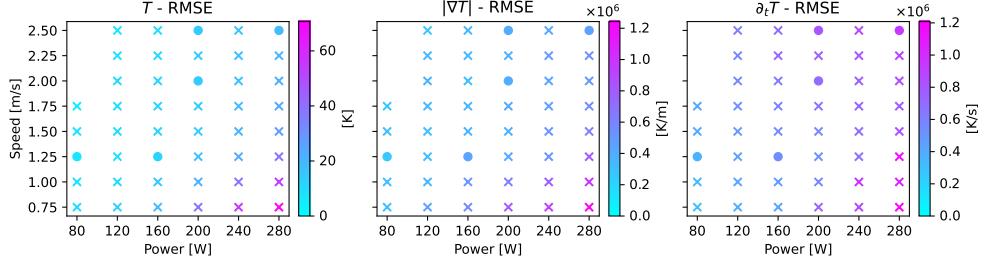


Fig. 6 MeltpoolINR: RMSE in the temperature field, its gradient, and the cooling rate at different laser power and scanning speeds for the initial substrate temperature of 380 K. Crosses denote training data, and circles denote test data.

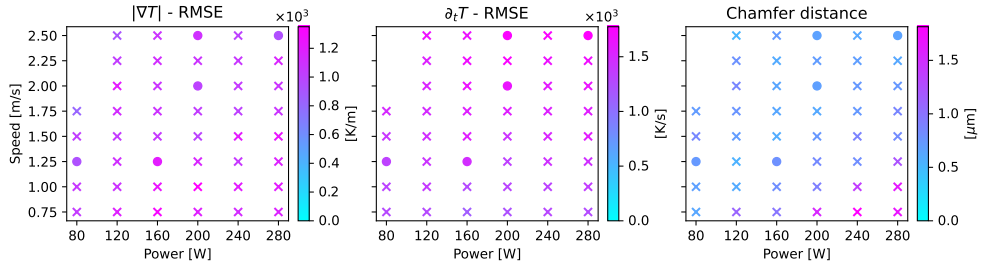


Fig. 7 MeltpoolINR: RMSE in the temperature gradient and in the cooling rate at the melt pool boundary together with the error in the melt pool boundary at different laser power and scanning speeds for the initial substrate temperature of 380 K. Crosses denote training data, and circles denote test data.

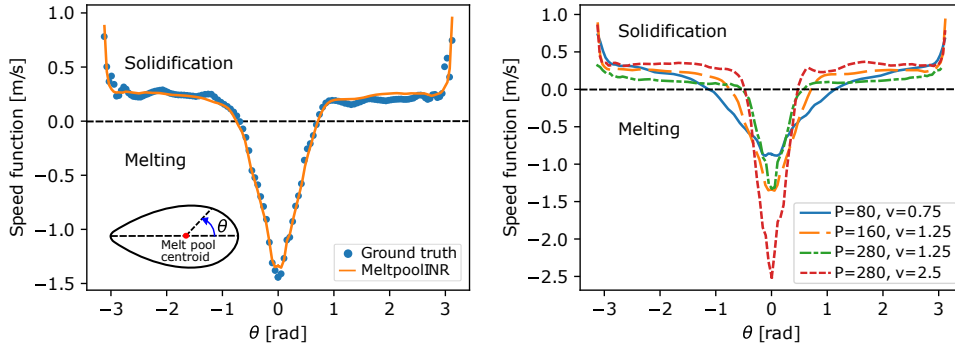


Fig. 8 MeltpoolINR: speed function at the melt pool boundary for a laser power of 160 W, a scanning speed of 1.25 m/s, and an initial substrate temperature of 380 K at time 202 μ s (left); Speed function at the melt pool boundary for four different combinations of process parameters (right).

pool boundary and to estimate the temperature gradient and cooling rate at the boundary. In contrast, MeltpoolINR does not require such interpolation. F exhibits sharper variation at the front (near $\theta = 0$) and back (near $\theta = \pm\pi$) of the melt pool boundary, where the curvature of the boundary is high. Away from these points, it

changes slowly. Additionally, $F > 0$ indicates the solidification rate. The variation of F with a change in the chosen process parameters is also illustrated in Figure 8. At the smallest laser power and scanning speed, F changes gradually from the front of the melt pool to the back. With increasing power and speed, the melt pool stretches and F plateaus in the two sections of the boundary. Near the front and the back of the melt pool, again F exhibits sharp changes. These variations in the solidification rate, which our model can infer, are crucial for understanding the microstructure evolution in LPBF.

Additionally, we estimate the melt pool length and aspect ratio and investigate their rate of change with respect to laser power, scanning speed, and initial substrate temperature at a given time. Figure 9 illustrates their variation with the laser power at

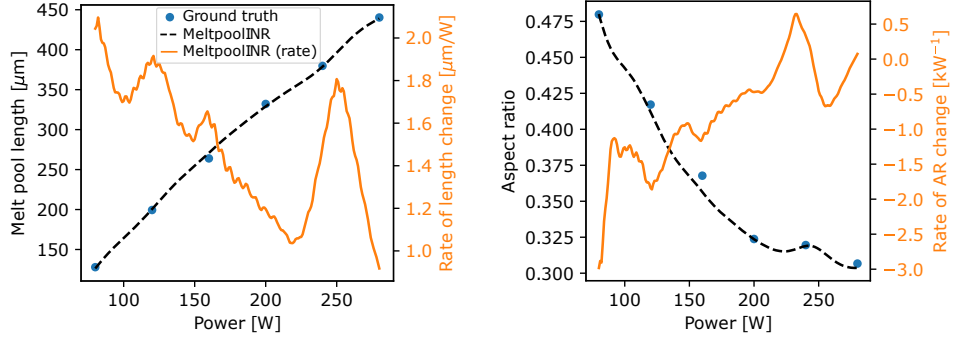


Fig. 9 MeltpoolINR: variation of the length and aspect ratio of the melt pool and their rate of change with respect to laser power for a scanning speed of 1.25 m/s and an initial substrate temperature of 380 K at time 202 μ s.

a given time, scanning speed, and substrate initial temperature. The values obtained from MeltpoolINR closely align with the ground truth. Increasing power leads to a significant increase in the melt pool length and a considerable decrease in the aspect ratio for most of the power range. The rate of increase of the length lies in a narrow range of values. The rate of change of the aspect ratio for higher values of power indicates that the aspect ratio does not change considerably with increasing power even though the melt pool length increases. This can be attributed to the qualitative change in the melt pool geometry between 240 W and 280 W at a scanning speed of 1.25 m/s observed in Figure E6.

Figure 10 shows the variation of the melt pool length and aspect ratio with respect to scanning speed at a given time, laser power, and substrate initial temperature. The length and aspect ratio decrease with increasing scanning speed. Compared to the case of laser power variation, the change in the length and aspect ratio over the complete range of scanning speed is considerably smaller. However, the rate of the length and aspect ratio change varies over a large range of values. Note that the maximum error in the length and aspect ratio prediction is $\approx 5\%$.

Figure 11 shows the variation of the melt pool length and aspect ratio with respect to substrate initial temperature at a given time, laser power, and scanning speed.

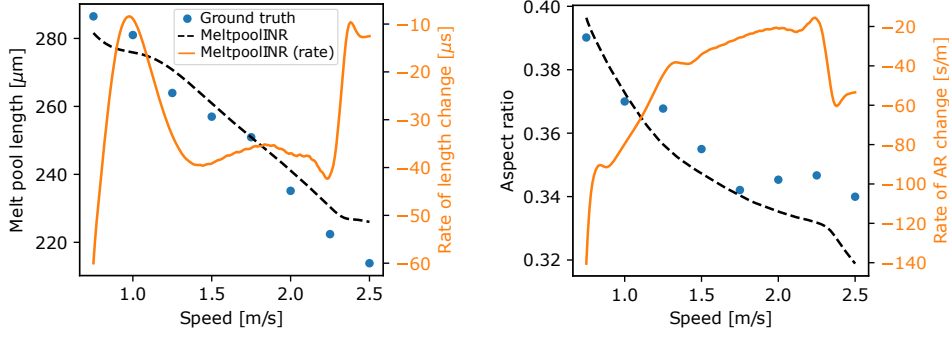


Fig. 10 MeltpoolINR: variation of the length and aspect ratio of the melt pool and their rate of change with respect to scanning speed for a laser power of 160 W and an initial substrate temperature of 380 K at time 202 μ s.

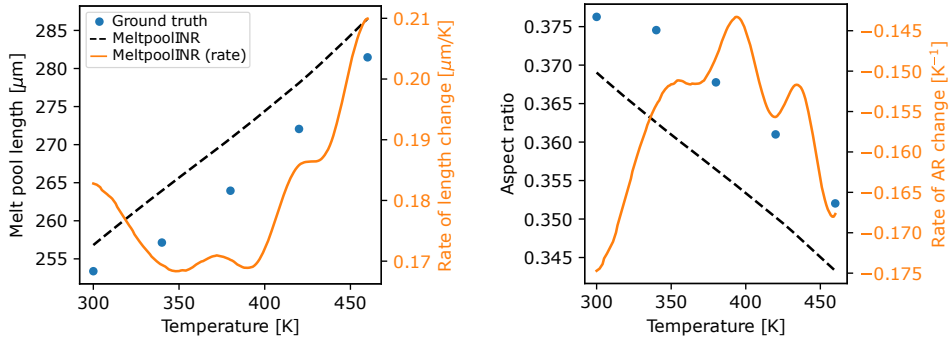


Fig. 11 MeltpoolINR: variation of the length and aspect ratio of the melt pool and their rate of change with respect to initial substrate temperature for a laser power of 160 W and a scanning speed of 1.25 m/s at time 202 μ s.

The length and aspect ratios increase with increasing substrate initial temperature. However, compared to the cases of the laser power and scanning speed variation, the length and aspect ratio are least sensitive to the variation of the substrate's initial temperature. Note that the maximum error in the length and aspect ratio prediction is $< 5\%$.

5 Discussion

Our aim was to develop a model that accurately predicts the temperature field, melt pool boundary, thermal gradient and cooling rate at the melt pool boundary, and the change in them due to a change in the process parameters in LPBF. We show that MeltpoolINR exhibits strong generalization capability and accurately predicts the temperature field, temperature gradient, and cooling rate as confirmed by Figure 4. The model also accurately predicts the melt pool boundary as shown in Figure 4. The implicit neural representation of the melt pool as a level set allows the prediction of the

melt pool evolution accurately as shown in Figure 8. This feature also facilitates the investigation of the dependence of the solidification rate on the process parameters. Furthermore, the model predicts the change in the melt pool geometry with a change in the process parameters in close agreement with the simulation results.

We have demonstrated the effectiveness of our approach in learning the top view of the temperature field, its gradient, and cooling rate in a single-track LPBF process. The desired extension to 3D requires the model to be trained on a dataset with 3D field information without any significant alteration to the model. Further research is needed to extend the model to multi-track printing.

6 Conclusions

In the LPBF process, the temperature field, its gradient, and cooling rate along with the melt pool morphology have a critical influence on the properties of fabricated parts. Their quick inference is necessary to model microstructure and residual stresses accurately. Additionally, optimizing the process parameters requires the rate of change of the temperature field and melt pool features with respect to the process parameters. We addressed these challenges in this work by developing and training a differentiable model based on MLPs with Fourier feature encoding. The model predicts a top view of the temperature field, its gradient, and the cooling rate. The accuracy of the prediction is demonstrated by comparison with predictions from a state-of-the-art CNN-based model trained on the same data. Furthermore, by implicitly representing the melt pool boundary as a level set, we quantify the solidification rate and predict the rate of change of the melt pool geometry with respect to the process parameters.

This study focused on learning the top view of fields in a single-track LPBF process to demonstrate the effectiveness of our approach. Future research can extend this framework to 3D geometries for multi-track printing scenarios.

Acknowledgements. The authors acknowledge the Swiss Data Science Center for funding the project under grant no. C21-07.

Appendix A Transformation of the frame of reference

x , y and t are the spatial and temporal coordinates in the fixed reference frame. We define ξ , y and t as the coordinates in the frame attached to the laser moving in the x -direction of the fixed frame such that

$$\xi = x - x_l, \tag{A1}$$

$$x_l = x_0 + vt, \tag{A2}$$

where v is the scanning speed, and x_0 is the position of the laser at $t = 0$. The temperature field is given by $T(x, y, t) = \tilde{T}(\xi, y, t)$. The derivatives in the two

frames are related by the material derivative as follows:

$$\frac{DT}{Dt} = \frac{\partial \tilde{T}}{\partial t} - v \frac{\partial \tilde{T}}{\partial \xi}. \quad (\text{A3})$$

Note that at steady state, $\frac{\partial \tilde{T}}{\partial t} = 0$. Hence $\frac{DT}{Dt} = -v \frac{\partial \tilde{T}}{\partial \xi}$. Furthermore, since material particles are stationary in the fixed frame, $\frac{DT}{Dt}$ is the time derivative in the fixed frame, i.e. $\frac{DT}{Dt} = \frac{\partial T}{\partial t}$. In our data, v is constant during a printing process. So, on using (A2), (A3) transforms to the following form:

$$\frac{\partial T}{\partial t} = v \left(\frac{\partial \tilde{T}}{\partial x_l} - \frac{\partial \tilde{T}}{\partial \xi} \right). \quad (\text{A4})$$

Appendix B Architecture of the CNN

Figure B1 shows the architecture of the CNN. Note that upsampling uses the bilinear algorithm. The stride of the convolution is set to be 1. Additionally, a padding of size 1 is added to the four boundaries of the input to a convolution layer by replicating the values at the corresponding boundaries.

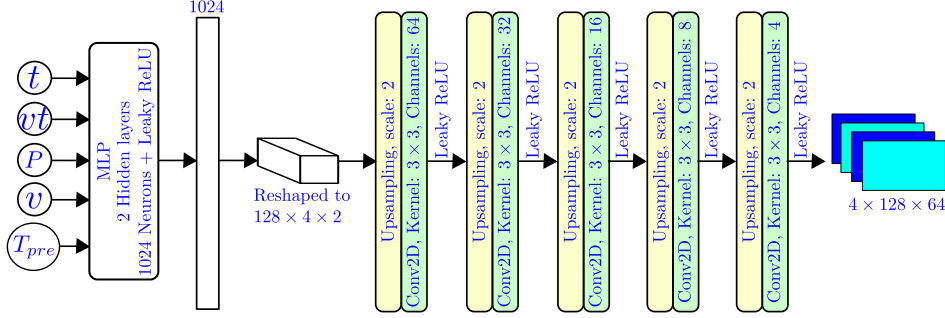


Fig. B1 Architecture of the CNN.

Appendix C Chamfer distance

Chamfer distance is a frequently used metric in Computer Vision to compute the distance between two point clouds. In order to calculate it, we resample the true melt pool boundary and the predicted melt pool boundary into two large point clouds \mathcal{C}_1 , \mathcal{C}_2 and then compute the Chamfer distance as follows:

$$d_{\text{Chamfer}} = \frac{1}{2N} \left(\sum_{x \in \mathcal{C}_1} \min_{y \in \mathcal{C}_2} \|x - y\|_2 + \sum_{y \in \mathcal{C}_2} \min_{x \in \mathcal{C}_1} \|y - x\|_2 \right) \quad (\text{C5})$$

Appendix D RMSE for the complete set of process parameters

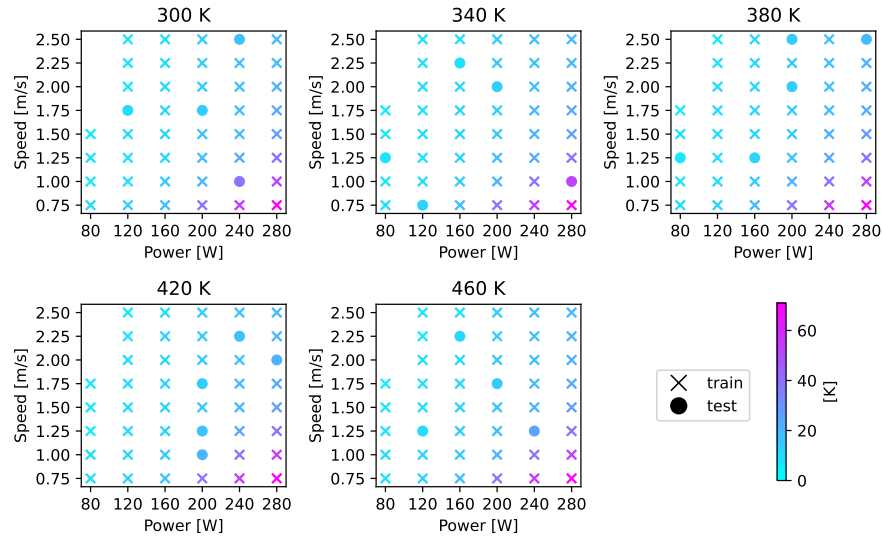


Fig. D2 MeltpoolINR: RMSE of the temperature field.

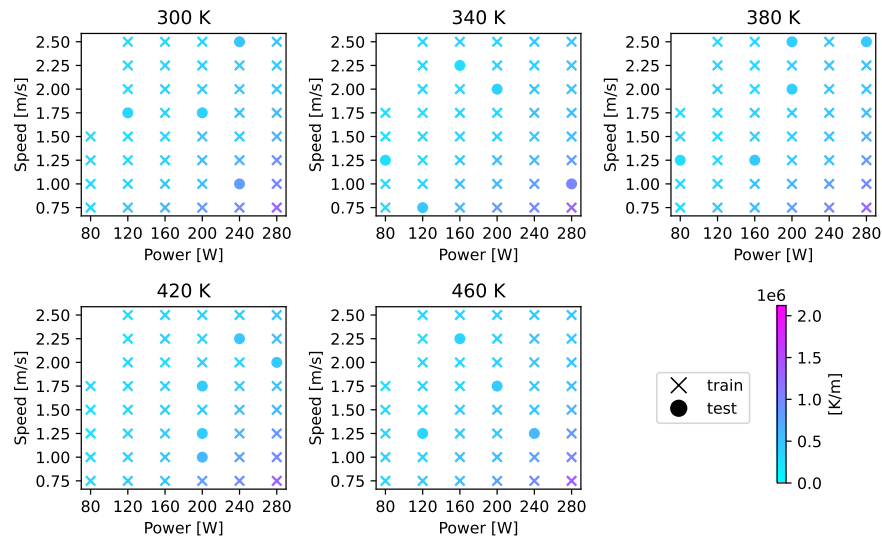


Fig. D3 MeltpoolINR: RMSE of the gradient of the temperature field.

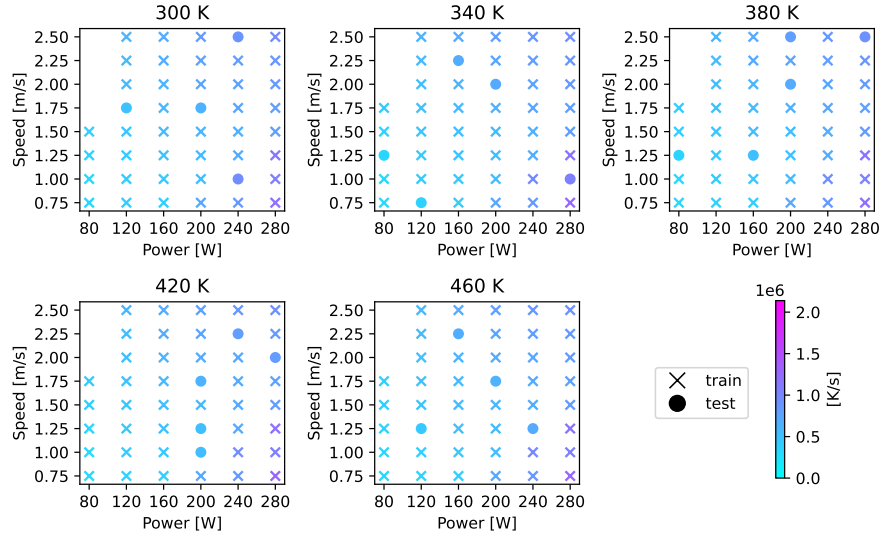


Fig. D4 MeltpoolINR: RMSE of the cooling rate.

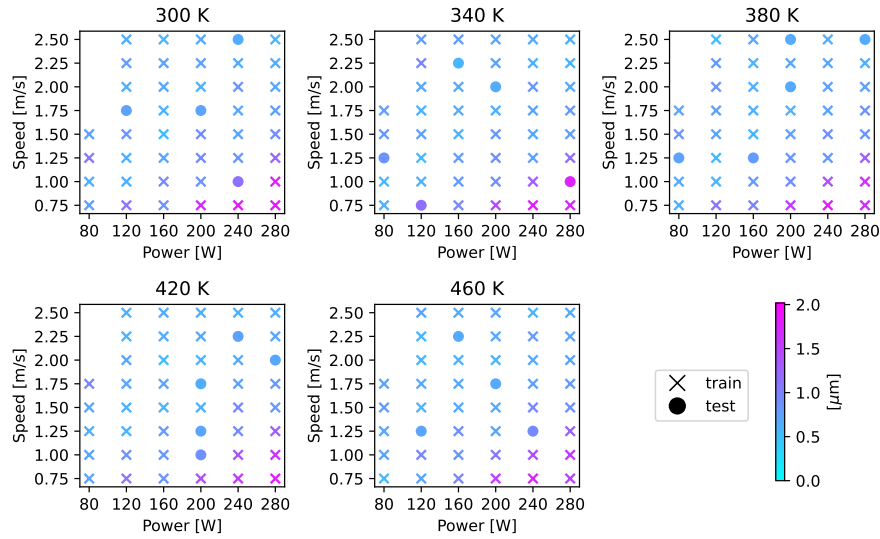


Fig. D5 MeltpoolINR: Error in the melt pool boundary measured as the Chamfer distance.

Appendix E Temperature field in the steady state

References

- [1] Attaran, M.: The rise of 3-d printing: The advantages of additive manufacturing over traditional manufacturing. *Business horizons* **60**(5), 677–688 (2017)

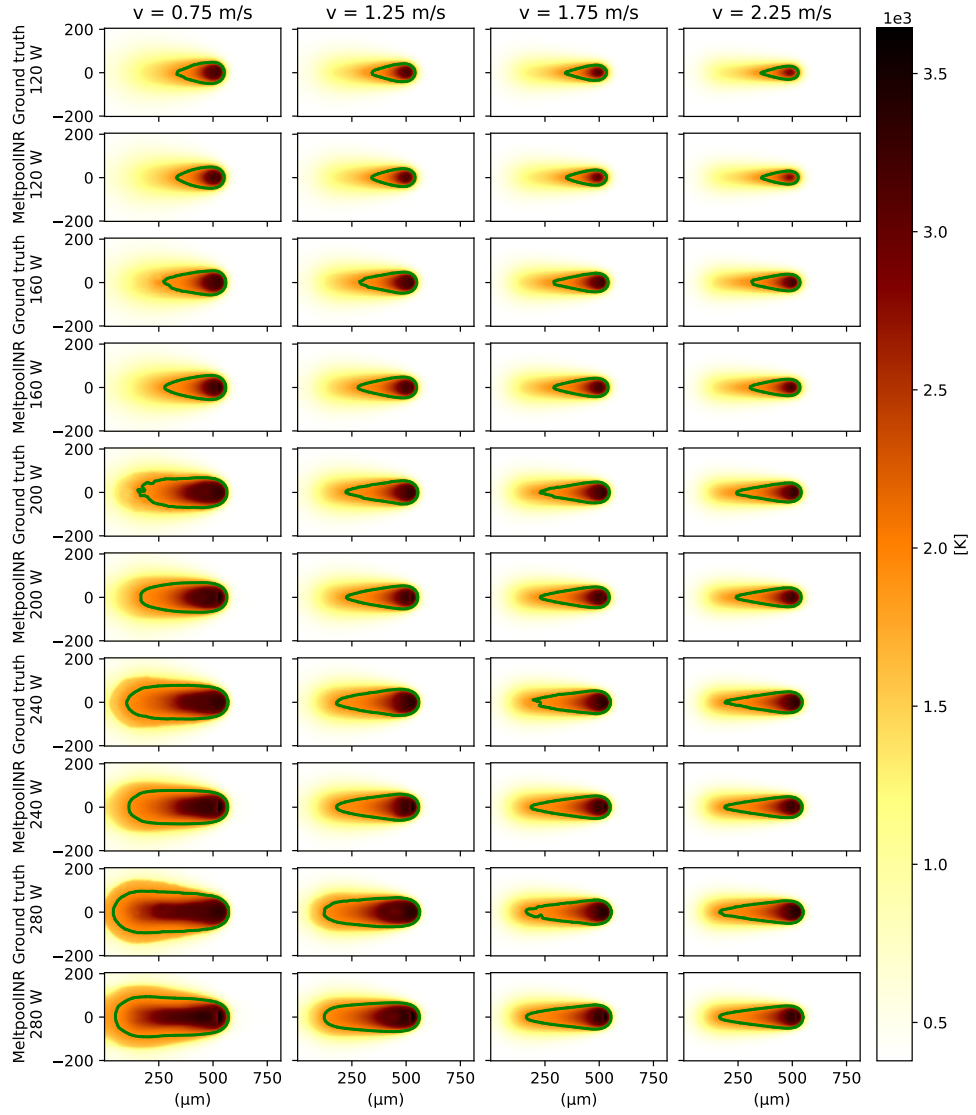


Fig. E6 The temperature field and melt pool boundary at time $202 \mu\text{s}$ for different laser power and velocities and an initial substrate temperature of 380 K .

- [2] Yadroitsev, I., Yadroitsava, I., Du Plessis, A., MacDonald, E. (eds.): *Fundamentals of Laser Powder Bed Fusion of Metals*. Elsevier, Amsterdam (2021)
- [3] Afrasiabi, M., Bambach, M.: Modelling and simulation of metal additive manufacturing processes with particle methods: A review. *Virtual and Physical Prototyping* **18**(1), 2274494 (2023)

- [4] King, W.E., Anderson, A.T., Ferencz, R.M., Hodge, N.E., Kamath, C., Khairallah, S.A., Rubenchik, A.M.: Laser powder bed fusion additive manufacturing of metals; physics, computational, and materials challenges. *Applied Physics Reviews* **2**(4) (2015)
- [5] Oliveira, J.P., LaLonde, A., Ma, J.: Processing parameters in laser powder bed fusion metal additive manufacturing. *Materials & Design* **193**, 108762 (2020)
- [6] Snow, Z., Nassar, A.R., Reutzel, E.W.: Invited review article: Review of the formation and impact of flaws in powder bed fusion additive manufacturing. *Additive Manufacturing* **36**, 101457 (2020)
- [7] Mostafaei, A., Zhao, C., He, Y., Ghiaasiaan, S.R., Shi, B., Shao, S., Shamsaei, N., Wu, Z., Kouraytem, N., Sun, T., *et al.*: Defects and anomalies in powder bed fusion metal additive manufacturing. *Current Opinion in Solid State and Materials Science* **26**(2), 100974 (2022)
- [8] Soundararajan, B., Sofia, D., Barletta, D., Poletto, M.: Review on modeling techniques for powder bed fusion processes based on physical principles. *Additive Manufacturing* **47**, 102336 (2021)
- [9] Jardin, R.T., Tuninetti, V., Tchuindjang, J.T., Duchêne, L., Hashemi, N., Tran, H.S., Carrus, R., Mertens, A., Habraken, A.M.: Optimizing laser power of directed energy deposition process for homogeneous aisi m4 steel microstructure. *Optics & Laser Technology* **163**, 109426 (2023)
- [10] Pham, T., Hoang, T., Tran, X., Fetni, S., Duchêne, L., Tran, H.S., Habraken, A.: A framework for the robust optimization under uncertainty in additive manufacturing. *Journal of Manufacturing Processes* **103**, 53–63 (2023)
- [11] McCann, R., Obeidi, M.A., Hughes, C., McCarthy, É., Egan, D.S., Vijayaraghavan, R.K., Joshi, A.M., Garzon, V.A., Dowling, D.P., McNally, P.J., *et al.*: In-situ sensing, process monitoring and machine control in laser powder bed fusion: A review. *Additive Manufacturing* **45**, 102058 (2021)
- [12] Wang, Q., Michaleris, P.P., Nassar, A.R., Irwin, J.E., Ren, Y., Stutzman, C.B.: Model-based feedforward control of laser powder bed fusion additive manufacturing. *Additive Manufacturing* **31**, 100985 (2020)
- [13] Rosenthal, D.: The theory of moving sources of heat and its application to metal treatments. *Transactions of the American Society of Mechanical Engineers* **68**(8), 849–865 (1946)
- [14] Yang, Y., Knol, M., Van Keulen, F., Ayas, C.: A semi-analytical thermal modelling approach for selective laser melting. *Additive Manufacturing* **21**, 284–297 (2018)

- [15] Markl, M., Körner, C.: Multiscale modeling of powder bed-based additive manufacturing. *Annual Review of Materials Research* **46**, 93–123 (2016)
- [16] Moges, T., Ameta, G., Witherell, P.: A review of model inaccuracy and parameter uncertainty in laser powder bed fusion models and simulations. *Journal of manufacturing science and engineering* **141**(4), 040801 (2019)
- [17] Luo, Z., Zhao, Y.: A survey of finite element analysis of temperature and thermal stress fields in powder bed fusion additive manufacturing. *Additive Manufacturing* **21**, 318–332 (2018)
- [18] Dunbar, A.J., Denlinger, E.R., Gouge, M.F., Michaleris, P.: Experimental validation of finite element modeling for laser powder bed fusion deformation. *Additive Manufacturing* **12**, 108–120 (2016)
- [19] Acharya, R., Sharon, J.A., Staroselsky, A.: Prediction of microstructure in laser powder bed fusion process. *Acta Materialia* **124**, 360–371 (2017)
- [20] Yu, G., Gu, D., Dai, D., Xia, M., Ma, C., Shi, Q.: On the role of processing parameters in thermal behavior, surface morphology and accuracy during laser 3d printing of aluminum alloy. *Journal of Physics D: Applied Physics* **49**(13), 135501 (2016)
- [21] Afrasiabi, M., Lüthi, C., Bambach, M., Wegener, K.: Multi-resolution sph simulation of a laser powder bed fusion additive manufacturing process. *Applied Sciences* **11**(7), 2962 (2021)
- [22] Fürstenau, J.-P., Wessels, H., Weißenfels, C., Wriggers, P.: Generating virtual process maps of slm using powder-scale sph simulations. *Computational Particle Mechanics* **7**(4), 655–677 (2020)
- [23] Lüthi, C., Afrasiabi, M., Bambach, M.: An adaptive smoothed particle hydrodynamics (sph) scheme for efficient melt pool simulations in additive manufacturing. *Computers & Mathematics with Applications* **139**, 7–27 (2023)
- [24] Zakirov, A., Belousov, S., Bogdanova, M., Korneev, B., Stepanov, A., Perepelkina, A., Levchenko, V., Meshkov, A., Potapkin, B.: Predictive modeling of laser and electron beam powder bed fusion additive manufacturing of metals at the mesoscale. *Additive Manufacturing* **35**, 101236 (2020)
- [25] Karniadakis, G.E., Kevrekidis, I.G., Lu, L., Perdikaris, P., Wang, S., Yang, L.: Physics-informed machine learning. *Nature Reviews Physics* **3**(6), 422–440 (2021)
- [26] Wang, P., Yang, Y., Moghaddam, N.S.: Process modeling in laser powder bed fusion towards defect detection and quality control via machine learning: The state-of-the-art and research challenges. *Journal of Manufacturing Processes* **73**, 961–984 (2022)

- [27] Mozaffar, M., Liao, S., Xie, X., Saha, S., Park, C., Cao, J., Liu, W.K., Gan, Z.: Mechanistic artificial intelligence (mechanistic-ai) for modeling, design, and control of advanced manufacturing processes: Current state and perspectives. *Journal of Materials Processing Technology* **302**, 117485 (2022)
- [28] Zhu, Q., Liu, Z., Yan, J.: Machine learning for metal additive manufacturing: predicting temperature and melt pool fluid dynamics using physics-informed neural networks. *Computational Mechanics* **67**, 619–635 (2021)
- [29] Liao, S., Xue, T., Jeong, J., Webster, S., Ehmann, K., Cao, J.: Hybrid thermal modeling of additive manufacturing processes using physics-informed neural networks for temperature prediction and parameter identification. *Computational Mechanics* **72**(3), 499–512 (2023)
- [30] Hosseini, E., Ghanbari, P.G., Müller, O., Molinaro, R., Mishra, S.: Single-track thermal analysis of laser powder bed fusion process: Parametric solution through physics-informed neural networks. *Computer Methods in Applied Mechanics and Engineering* **410**, 116019 (2023)
- [31] Chen, F., Yang, M., Yan, W.: Data-driven prognostic model for temperature field in additive manufacturing based on the high-fidelity thermal-fluid flow simulation. *Computer Methods in Applied Mechanics and Engineering* **392**, 114652 (2022)
- [32] Ren, K., Chew, Y., Zhang, Y., Fuh, J., Bi, G.: Thermal field prediction for laser scanning paths in laser aided additive manufacturing by physics-based machine learning. *Computer Methods in Applied Mechanics and Engineering* **362**, 112734 (2020)
- [33] Pham, T.Q.D., Hoang, T.V., Van Tran, X., Pham, Q.T., Fetni, S., Duchêne, L., Tran, H.S., Habraken, A.-M.: Fast and accurate prediction of temperature evolutions in additive manufacturing process using deep learning. *Journal of Intelligent Manufacturing* **34**(4), 1701–1719 (2023)
- [34] Hemmasian, A., Ogoke, F., Akbari, P., Malen, J., Beuth, J., Farimani, A.B.: Surrogate modeling of melt pool temperature field using deep learning. *Additive Manufacturing Letters* **5**, 100123 (2023)
- [35] Sideris, I., Crivelli, F., Bambach, M.: Gpyro: uncertainty-aware temperature predictions for additive manufacturing. *Journal of Intelligent Manufacturing* **34**(1), 243–259 (2023)
- [36] Bertoli, U.S., Guss, G., Wu, S., Matthews, M.J., Schoenung, J.M.: In-situ characterization of laser-powder interaction and cooling rates through high-speed imaging of powder bed fusion additive manufacturing. *Materials & Design* **135**, 385–396 (2017)
- [37] Lienert, T., Siewert, T., Babu, S., Acoff, V.: Fundamentals of weld solidification.

ASM handbook **6**, 69–114 (2011)

- [38] Wei, H., Mazumder, J., DebRoy, T.: Evolution of solidification texture during additive manufacturing. *Scientific reports* **5**(1), 16446 (2015)
- [39] DebRoy, T., Wei, H., Zuback, J., Mukherjee, T., Elmer, J., Milewski, J., Beese, A.M., Wilson-Heid, A.d., De, A., Zhang, W.: Additive manufacturing of metallic components—process, structure and properties. *Progress in Materials Science* **92**, 112–224 (2018)
- [40] Kruth, J.-P., Deckers, J., Yasa, E., Wauthlé, R.: Assessing and comparing influencing factors of residual stresses in selective laser melting using a novel analysis method. *Proceedings of the institution of mechanical engineers, Part B: Journal of Engineering Manufacture* **226**(6), 980–991 (2012)
- [41] Li, C., Liu, Z., Fang, X., Guo, Y.: Residual stress in metal additive manufacturing. *Procedia Cirp* **71**, 348–353 (2018)
- [42] Fang, Z.-C., Wu, Z.-L., Huang, C.-G., Wu, C.-W.: Review on residual stress in selective laser melting additive manufacturing of alloy parts. *Optics & Laser Technology* **129**, 106283 (2020)
- [43] Levkulich, N., Semiatin, S., Gockel, J., Middendorf, J., DeWald, A., Klingbeil, N.: The effect of process parameters on residual stress evolution and distortion in the laser powder bed fusion of ti-6al-4v. *Additive Manufacturing* **28**, 475–484 (2019)
- [44] Kou, S.: *Welding metallurgy*. New Jersey, USA **431**(446), 223–225 (2003)
- [45] Blecher, J., Palmer, T., DebRoy, T.: Solidification map of a nickel-base alloy. *Metallurgical and Materials Transactions A* **45**, 2142–2151 (2014)
- [46] Mildenhall, B., Srinivasan, P.P., Tancik, M., Barron, J.T., Ramamoorthi, R., Ng, R.: Nerf: Representing scenes as neural radiance fields for view synthesis. *Communications of the ACM* **65**(1), 99–106 (2021)
- [47] Tancik, M., Srinivasan, P., Mildenhall, B., Fridovich-Keil, S., Raghavan, N., Singhal, U., Ramamoorthi, R., Barron, J., Ng, R.: Fourier features let networks learn high frequency functions in low dimensional domains. *Advances in neural information processing systems* **33**, 7537–7547 (2020)
- [48] Czarnecki, W.M., Osindero, S., Jaderberg, M., Swirszcz, G., Pascanu, R.: Sobolev training for neural networks. *Advances in neural information processing systems* **30** (2017)
- [49] Gingold, R.A., Monaghan, J.J.: Smoothed particle hydrodynamics: theory and application to non-spherical stars. *Monthly notices of the royal astronomical society* **181**(3), 375–389 (1977)

- [50] Lucy, L.B.: A numerical approach to the testing of the fission hypothesis. *The astronomical journal* **82**, 1013–1024 (1977)
- [51] Lin, Y., Lüthi, C., Afrasiabi, M., Bambach, M.: Enhanced heat source modeling in particle-based laser manufacturing simulations with ray tracing. *International Journal of Heat and Mass Transfer* **214**, 124378 (2023)
- [52] Cummins, S., Cleary, P.W., Delaney, G., Phua, A., Sinnott, M., Gunasegaram, D., Davies, C.: A coupled dem/sph computational model to simulate microstructure evolution in ti-6al-4v laser powder bed fusion processes. *Metals* **11**(6) (2021)
- [53] Wendland, H.: Piecewise polynomial, positive definite and compactly supported radial functions of minimal degree. *Advances in Computational Mathematics* **4**(1), 389–396 (1995)
- [54] Garbin, S.J., Kowalski, M., Johnson, M., Shotton, J., Valentin, J.: Fastnerf: High-fidelity neural rendering at 200fps. In: *Proceedings of the IEEE/CVF International Conference on Computer Vision*, pp. 14346–14355 (2021)
- [55] Ogoke, F., Lee, W., Kao, N.-Y., Myers, A., Beuth, J., Malen, J., Barati Farimani, A.: Convolutional neural networks for melt depth prediction and visualization in laser powder bed fusion. *The International Journal of Advanced Manufacturing Technology*, 1–16 (2023)
- [56] Sethian, J.A., *et al.*: *Level Set Methods and Fast Marching Methods* vol. 98. Cambridge UP: Cambridge, Cambridge (1999)